BMC Medical Imaging

RESEARCH

Open Access

An artificial intelligence algorithm for the detection of pulmonary ground-glass nodules on spectral detector CT: performance on virtual monochromatic images

Zhong-Yan Ma[1†], Hai-lin Zhang[2†], Fa-jin Lv[3], Wei Zhao[1], Dan Han[1], Li-chang Lei[1], Qin Song[1], Wei-wei Jing[3], Hui Duan[1*†] and Shao-Lei Kang[1,3*†]

Abstract

Background This study aims to assess the performance of an established an AI algorithm trained on conventional polychromatic computed tomography (CT) images (CPIs) to detect pulmonary ground-glass nodules (GGNs) on virtual monochromatic images (VMIs), and to screen the optimal virtual monochromatic energy for the clinical evaluation of GGNs.

Methods Non-enhanced chest SDCT images of patients with pulmonary GGNs in our clinic from January 2022 to December 2022 were continuously collected: adenocarcinoma in situ (AIS, $n=40$); minimally invasive adenocarcinoma (MIA, $n=44$) and invasive adenocarcinoma (IAC, $n=46$). A commercial CAD system based on deep convolutional neural networks (DL-CAD) was used to process the CPIs, 40, 50, 60, 70, and 80 keV monochromatic images of 130 spectral CT images. AI-based histogram parameters by logistic regression analysis. The diagnostic performance was evaluated by the receiver operating characteristic (ROC) curves, and Delong's test was used to compare the CPIs group with the VMIs group.

Results When distinguishing IAC from MIA, the diagnostic efficiency of total mass was obtained at 80 keV, which was superior to those of other energy levels ($P<0.05$). And Delong's test indicated that the differences between the area-under-the-curve (AUC) values of the CPIs group and the VMIs group were not statistically significant ($P>0.05$).

Conclusion The AI algorithm trained on CPIs showed consistent diagnostic performance on VMIs. When pulmonary GGNs are encountered in clinical practice, 80 keV could be the optimal virtual monochromatic energy for the identification of preoperative IAC on a non-enhanced chest CT.

†Zhong-Yan Ma and Hai-lin Zhang contributed equally to this work.

†Hui Duan and Shao-Lei Kang contributed equally to this study as co-corresponding authors.

*Correspondence:
Hui Duan
huierxiao1122@163.com
Shao-Lei Kang
shaolei_kang@foxmail.com
Full list of author information is available at the end of the article

Keywords Pulmonary ground-glass nodule, Artificial intelligence, Deep learning, Dual-layer detector spectral, Computed tomography, Virtual monochromatic images

Introduction

Lung cancer ranks second for cancer incidence and first for cancer mortality [1]. Early diagnosis and treatment of lung cancer can significantly reduce lung cancer-related mortality. Pulmonary ground-glass nodules (GGNs) are considered to be the most common manifestation of early lung adenocarcinoma [2, 3]. With the improvement of high-resolution computed tomography (HRCT) and health awareness, more and more ground glass lesions are found [4, 5]. Pathologically, lung adenocarcinomas can be divided into adenocarcinomas in situ (AIS), minimally invasive adenocarcinomas (MIA), invasive adenocarcinomas (IAC) [6, 7]. Studies have shown that the 5-year survival rate of patients with AIS and MIA can reach or approach 100% [8], and accurate and rapid differential diagnosis is essential for both their treatment and prognosis. However, it is difficult to differentiate GGNs due to their small size, tenuous texture, less obvious enhancement characteristics, and unprominent morphological characteristics on imaging to differentiate benign from malignant GGNs [9].

Artificial intelligence (AI) is increasingly used in medical imaging to try to alleviate the growing workload of radiologists. An AI algorithm based on deep learning can not only identify, classify, reconstruct, and reduce the noise of pulmonary nodules, extract the main features of pulmonary nodules from imaging images, and predict the early detection of pulmonary nodules and the judgment of benign and malignant lesions [10, 11], but also improve the work efficiency of cardiothoracic imaging doctors and reduce the missed diagnosis and misdiagnosis of doctors [12].

Dual-layer detector spectral computed tomography (SDCT) can through retrospective reconstruction virtual single energy images (VMIs), so as to improve the signal-to-noise ratio (SNR) and contrast to noise ratio (CNR) [13–15]. Some studies demonstrated that VMIs at 60 keV or 70 keV provided the best combination of subjective and objective image quality in the evaluation of lung cancer [16, 17]. Nevertheless, due to different appearances on VMIs, the performance of AI trained on conventional CT images may worsen.

However, the altered image appearance caused by using different imaging techniques can influence the performance of AI algorithms. A recently published systematic review by Wu Z et al aimed to compare the quality and accuracy of lung cancer risk prediction models based on pulmonary nodules [18]. They found that the existing models showed good discrimination for identifying high-risk pulmonary nodules but lacked external validation. More researches are required to improve the quality of deep learning models. Currently, no research has been conducted on the use of AI to detect pulmonary GGNs on VMIs. Therefore, this study aims to assess the performance of an established an AI algorithm trained on conventional polychromatic computed tomography (CT) images (CPIs) to detect pulmonary GGNs on VMIs and to screen the optimal virtual monochromatic energy for the clinical evaluation of GGNs.

Materials and methods

Study participants

This study conformed to the Declaration of Helsinki on Human Research Ethics standards and was approved by the institutional review board of the First Affiliated Hospital of Kunming Medical University (No.2022-L179). The need for written informed consent was waived because of the retrospective study. A total of 130 patient cases were identified, consisting of 47 males and 83 females with a mean age of 51.13 ± 12.547 years (range, 19–86 years). Non-enhanced chest SDCT images of patients with pulmonary GGNs in our clinic from January 2022 to December 2022 were continuously collected. The inclusion criteria were: GGNs detected by SDCT and with pathological results obtained by clinical surgery (include 40 cases of adenocarcinoma in situ, AIS; 44 cases of minimally invasive adenocarcinoma, MIA; and 46 cases of invasive adenocarcinoma, IAC); available thin-section chest computed tomography (CT) images (slice thickness, ≤ 1 mm). The exclusion criteria were: 1) CT images with motion artifacts; 2) other lung diseases such as pneumoconiosis, tuberculosis, or pneumonia; 3) a previous history of cancer; and 4) no definite diagnosis could be made by pathology.

CT Screening and SDCT image reconstruction

Chest scan examinations were performed on a dual-layer spectral detector CT (IQon Spectral CT, Philips Healthcare). All unenhanced CT acquisitions were scanned in the supine position, head first. To ensure that all lung tissues were covered, scans were performed from the thoracic inlet to the costophrenic. Scanning parameters: tube voltage 120 kV, automatic tube current modulation, rotation speed 0.33 s/rot; helical pitch 0.938, image reconstruction matrix 512×512, layer thickness 1 mm,

layer spacing 0.7 mm. Lung window (width, 1500HU; level, − 400 HU) was used for group conventional CT image analysis. VMIs (Spectral B, level 3, range: 40–80 keV, increment of 10 keV) were reconstructed. These series were then sent to the deep learning-based computer-aided diagnosis (DL-CAD) system.

Evaluation by a deep learning-based computeraided diagnosis (DL-CAD) system

A commercial CAD system (Deepwise 20201130fix1a, Hangzhou Deepwise, and PHD Technology Co., Ltd.) based on deep convolutional neural networks (DL-CAD) was used to process the 40, 50, 60, 70, and 80 keV monochromatic images of 130 spectral CT images. The AI-based histogram parameters included: total volume, total mass, and mean CT value. Moreover, kurtosis, skewness, entropy, three-dimensional (3D) CT long diameter (the largest diameter of the whole 3D lesion), superficial area (the surface area of the largest contour of the lesion), maximum section area (the number of the sections showing the largest lesion contour), and sphericity (score range, 0–1 [the greater the similarity between the lesion and a sphere in 3D mode, the higher the score]).

Reference standard

The reference standard was established in a previous study, which included a reading by the attending radiologist and a consensus between three cardiothoracic radiologists (H.D., L.S.K. and W.Z.) with more than 10 years of work experience aided by the DL-CAD application. Subsequently, after the AI analysis, the discrepant cases were re-evaluated by two radiologists (Y.Z.M., L.H.Z.) with more than 20 years of work experience with access to the CPIs and VMIs AI outputs and the previously determined consensus outcome. Final decisions on the reference standard were taken in consensus.

Statistical analysis

SPSS Version 26.0 statistical analysis software (IBM, Armonk, New York, USA) and R software (version 3.5.1, www.r-project.org) were used to analyze the results and plot curves. The counting data was expressed as the number of cases, which was tested by the chi-square test. The Shapiro–Wilk test was used to test the quantitative data, which was in accordance with normal distribution and expressed as mean ± standard deviation (mean ± SD). The quantitative data with a skewed distribution was expressed as the median and quartile M (Q_{25}, Q_{75}). The two-sample t-test or Mann–Whitney U test was performed to assess the differences in quantitative data. The univariate and multivariate logistic regression analyses were used to determine the independent predictors of invasiveness for the variables with statistical significance. The area-under the curve (AUC), sensitivity, specificity, and diagnostic threshold or optimal cutoff value of all the independent predictors were analyzed and calculated by a receiver operating characteristic (ROC) curve. Delong's test was used to compare the CPIs group with the VMIs group.

Results

Patient inclusion

All spectral detector CT examinations were performed without any complications or relevant motion artifacts. A total of 130 GGNs were detected in 130 patients in this study (Fig. 1). Among the 130 GGNs, 46 cases of IAC, 44 cases of MIA, and 40 cases of AIS. The final study group consisted of 130 patients (51.13 ± 12.547 years; range, 19–86 years), comprised of 47 male (52.11 ± 13.639 years; range, 19–86 years) and 83 female (50.58 ± 11.936 years; range, 23–75 years) patients. Table 1 shows their clinical

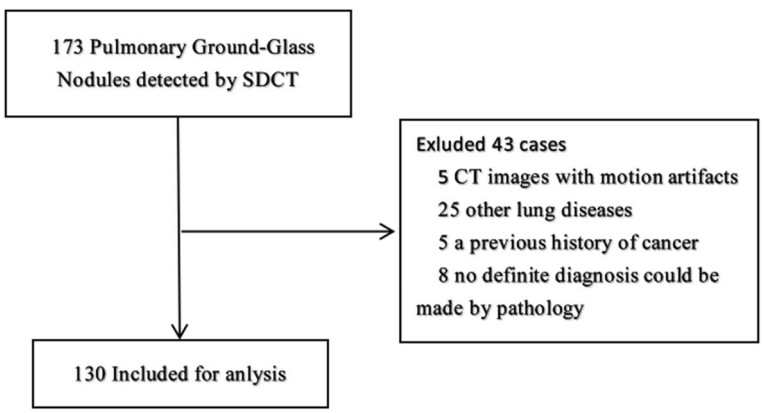

Fig. 1 Flowchart of patient selection

Table 1 Comparison of clinical characteristics and AI quantitative parameters of GGNs in the convention group

Characteristics	MIA($n=44$)	IAC($n=46$)	*P* value	MIA($n=44$)	AIS ($n=40$)	*P* value
Sex(male)	15(34.1%)	17(37.0%)	0.776[a]	15(34.1%)	15(37.5%)	0.810[a]
Age (years)	47.75 ± 12.10	58.02 ± 10.42	0.000[c]	47.75 ± 12.10	46.93 ± 12.12	0.756[c]
Total volume (mm^3)	220.80(140.07, 333.98)	575.25(296.83, 1563.23)	0.000[b]	220.80(140.07, 333.98)	158.65(105.73, 241.59)	0.029[b]
Total mass(mg)	67.20(45.53, 126.45)	237.65(128.43, 595.65)	0.000[b]	67.20(45.53, 126.45)	49.85(28.48, 77.25)	0.024[b]
Mean CT value (HU)	-690.95(717.55, -597.40)	-595.20(-687.80, -526.13)	0.001[b]	-690.95(717.55, -597.40)	-701.70(-742, -644)	0.134[b]
Maximum section area (mm^2)	33.26(25.93, 49.76)	71.48(42.14, 135.93)	0.000[b]	33.26(25.93, 49.76)	25.59(18.71, 34.46)	0.021[b]
Superficial area (mm^2)	168.45(109.038, 221.26)	311.07(207.09, 709.66)	0.000[b]	168.45(109.04, 221.26)	136.42(94.41, 182.67)	0.065[b]
3D long diameter (mm)	8.35(7.32, 10.68)	13.26(9.91, 17.75)	0.000[b]	8.35(7.32, 10.68)	7.19(6.26, 8.69)	0.009[b]
Sphericity	1(1, 1)	1(0.91, 1)	0.001[b]	1(1, 1)	1(1, 1)	0.825[b]
Kurtosis	7.33(4.67, 12.61)	7.23(4.82, 8.52)	0.990[b]	7.33(4.67, 12.61)	7.27(3.41, 11.79)	0.778[b]
Skewness	-2.01(-2.88, -0.89)	-1.95(-2.39, -1.57)	0.631[b]	-2.01(-2.88, -0.89)	-2.01 ± 1.48	0.993[b]
Entropy	7.96 ± 0.76	9.29 ± 1.162	0.000[c]	7.96 ± 0.76	7.62 ± 0.95	0.073[c]

AIS Adenocarcinomas in situ, *MIA* Minimally invasive adenocarcinoma, *IAC* Invasive adenocarcinoma, *GGNs* Pulmonary ground-glass nodules, *AI* Artificial intelligence, *CT* Computed tomography, *3D* Three-dimensional

[a] *P*-values were calculated by chi-square test

[b] *P*-values were calculated by Mann–Whitney U test

[c] *P*-value was calculated by two-sample t-test

characteristics and AI histogram parameters in the CPIs group. The variables other than sex, kurtosis, and skewness showed significant differences between MIA and IAC ($P<0.05$). The variables include total volume, total mass, maximum section area, and 3D long diameter showed significant differences between MIA and IAC ($P<0.05$).

Models building

The results of the univariate and multivariate logistic regression analyses for risk predictors for IAC or MIA in the CPIs group are shown in Table 2 and Table 2S. In the univariate analysis, maximum CT value and 3D long diameter were the risk predictors for MIA ($P<0.05$). In addition, the variables other than the kurtosis and skewness showed significant differences between MIA and IAC ($P<0.05$). Then these variables were analyzed by multivariate logistic regression analysis with the enter method. As a result, total mass [odds ratio (OR) 1.02, 95% confidence interval (CI) 1.002—1.038, $P=0.029$] was the independent predictor for IAC. And 3D long diameter (OR 1.61, 95% CI 1.021—2.523, $P=0.04$) was the independent predictor for MIA. Hence, 3D long diameter, total mass, total volume, and entropy were analyzed and calculated by a ROC curve as follows.

Table 2 Risk predictors for IAC in the univariate and multivariate logistic regression analysis

Variable	Univariate analysis		Multivariate analysis	
	OR (95% CI)	*P* value	OR (95% CI)	*P* value
Total volume (mm^3)	1.005(1.002—1.008)	0.001	—	—
Total mass(mg)	1.017(1.009—1.026)	0.000	1.02(1.002—1.038)	0.029
Maximum CT value (HU)	1.004(1.002—1.006)	0.000	—	—
Mean CT value (HU)	1.008(1.003—1.012)	0.002	—	—
Maximum section area (mm^2)	1.052(1.026—1.079)	0.000	1.014(0.957—1.074)	0.635
Superficial area (mm^2)	1.01(1.005—1.016)	0.000	—	—
3D long diameter (mm)	1.53(1.261—1.857)	0.000	1.004(0.617—1.633)	0.988
Kurtosis	1.005(0.965—1.046)	0.826	—	—
Skewness	0.897(0.661—1.216)	0.483	—	—
Entropy	5.058(2.375—10.772)	0.000	0.527(0.097—2.845)	0.456

IAC Invasive adenocarcinoma, *CT* Computed tomography, *3D* Three-dimensional, *OR* Odds ratio, *CI* Confidence interval

Diagnostic performance of AI quantitative parameters on VMIs

Among the multiple quantitative parameters, the four parameters with the highest diagnostic efficiency to distinguish between MIA and IAC were total $mass_{80kev}$, total $volume_{80kev}$, 3D long $diameter_{80kev}$ and $entropy_{80kev}$ (AUC = 0.871, 95% CI 0.798–0.932, $P < 0.001$; AUC = 0.846, 95% CI 0.766–0.917, $P < 0.001$; AUC = 0.858, 95% CI 0.781–0.924, $P = 0.010$, and AUC = 0.840, 95% CI 0.758–0.912, $P < 0.001$; respectively) (Table 3 and Table 3S, Fig. 2). The diagnostic efficiency of the total $mass_{80kev}$, total $mass_{70kev}$, total $mass_{60kev}$, total $mass_{50kev}$, total $mass_{convention}$ and total $mass_{40kev}$ were 0.871, 0.869, 0.867, 0.866, 0.862, and 0.851, respectively ($P < 0.05$), decreasing in turn. When the cut-off value of total $mass_{80kev}$ was 114.90, the sensitivity was 82.60%, the specificity was 77.30%, and the maximum Youden index was 0.599. The diagnostic efficiency of the total $volme_{80kev}$, total $volme_{70kev}$, total $volme_{60kev}$, total $volme_{50kev}$, total $volume_{convention}$ and total $volme_{40kev}$ were 0.846, 0.842, 0.843, 0.837, 0.823, and 0.807, respectively (for all, $P < 0.05$), decreasing in turn. When the cut-off value of total $volume_{80kev}$ was 276.45, the sensitivity, specificity, and maximum Youden index were 82.60%, 72.70%, 0.553, respectively (Table 3). And Delong's test indicated that the differences between the AUC values of the CPIs group and the VMIs group were not statistically significant ($P > 0.05$) (Table 3, Fig. 3). In addition, 3D long $diameter_{80kev}$ had the highest diagnostic efficiency in differentiating MIA from AIS (AUC = 0.665, 95% CI 0.790–0.909, $P < 0.001$) (Table 4, Fig. 4). When the cut-off value of 3D long $diameter_{80kev}$ was 7.37, the sensitivity, specificity, and the maximum Youden index were 70.50%, 65.00%, and 0.355, respectively (Table 4). And Delong's test indicated that the differences between the AUC values of the CPIs group and the VMIs group were not statistically significant (for all, $P > 0.05$) (Table 4, Fig. 5). In general, when distinguishing IAC from MIA, the diagnostic efficiencies of total mass and total volume were obtained at 80 keV, which were superior to those of other energy levels (for all, $P < 0.05$).

Discussion

The aim of this study was to assess whether an AI algorithm developed to detect pulmonary GGNs could be used on VMIs reconstructed from SDCT data, despite the fact that the algorithm was trained on CPIs. We found that the diagnostic performance of the AI algorithm that was trained on CPIs did not drop significantly on VMIs, reassuring its use in clinical practice. Logistic multivariable analysis indicated that total mass and total volume were risk predictors for IAC, and 3D long diameter was a risk predictor for MIA. In addition, when pulmonary GGNs are encountered in clinical practice, 80 keV could be the optimal virtual monochromatic energy for the identification of preoperatively IAC on a non-enhanced chest CT.

Artificial intelligence with stable performance on VMIs

Our findings that the diagnostic accuracy of an AI algorithm trained on CPIs was similar to that of VMIs have not before been shown in the literature, and it could be comforting for its usage in clinical practice as technology innovation in CT advances. Several studies have assessed

Table 3 ROC curve analysis for identifying IAC from MIA in convention group and VMIs group

		AUC	95% CI	*P* value	Sensitivity	Specificity	Youden index	Cutoff value	DeLong test (vs. Convention)
Total mass	Convention	0.862	0.790–0.926	0.000	82.60%	75.00%	0.576	120.65	—
	80	0.871	0.798–0.932	0.000	82.60%	77.30%	0.599	114.90	0.11
	70	0.869	0.798–0.932	0.000	82.60%	79.50%	0.621	117.35	0.24
	60	0.867	0.796–0.930	0.000	76.10%	84.10%	0.602	128.35	0.32
	50	0.866	0.794–0.928	0.000	76.10%	81.80%	0.579	125.85	0.48
	40	0.851	0.776–0.919	0.000	78.30%	77.30%	0.556	117.40	0.24
Total volume									
	Convention	0.823	0.736–0.899	0.000	69.60%	81.80%	0.514	359.12	—
	80	0.846	0.766–0.917	0.000	82.60%	72.70%	0.553	276.45	0.01
	70	0.842	0.759–0.914	0.000	82.60%	70.50%	0.531	263.84	0.03
	60	0.843	0.760–0.914	0.000	71.70%	81.80%	0.535	322.91	0.02
	50	0.837	0.752–0.910	0.000	71.70%	81.80%	0.535	325.48	0.13
	40	0.807	0.719–0.888	0.000	71.70%	77.30%	0.49	312.16	0.23

MIA Minimally invasive adenocarcinoma, *IAC* Invasive adenocarcinoma, *VMIs* Virtual monochromatic images, *ROC* Receiver operating characteristic, *AUC* Area under curve, *CI* Confidence interval

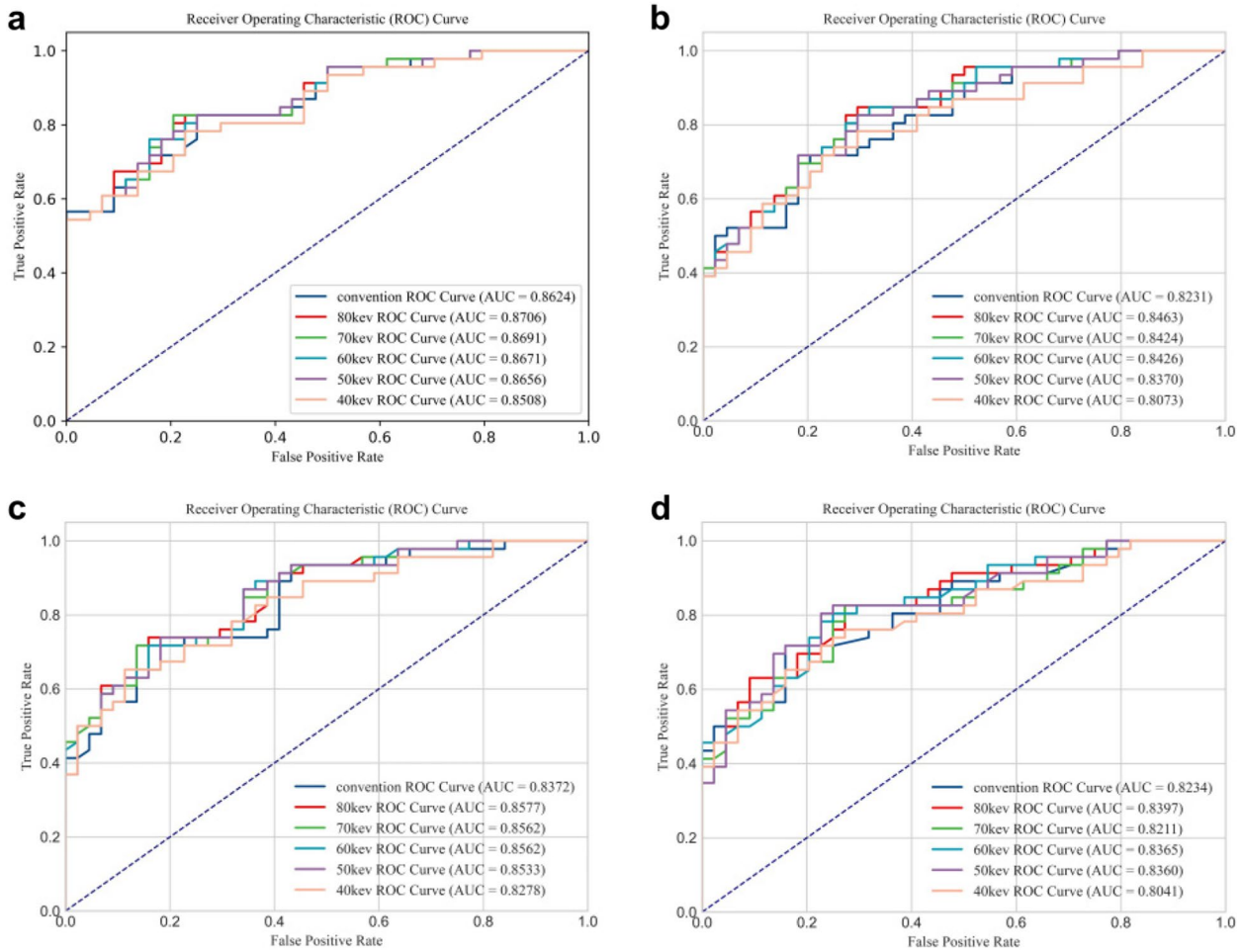

Fig. 2 Evaluation and verification of the IAC. **a** ROC curves for total mass in the CPIs group and VMIs group. **b** ROC curves for total volume in the CPIs group and VMIs group. **c** ROC curves for entropy in the CPIs group and VMIs group. **d** ROC curves for 3D long diameter in the CPIs group and VMIs group. IAC, invasive adenocarcinomas; ROC, receiver operating charcteristic; CPIs, computed tomography images; VMIs, virtual monochromatic images; 3D, three-dimensional

the reproducibility of AI algorithms' diagnostic accuracy. The majority of the AI algorithms used in this research indicated a decrease in performance on external data [19]. Delong's test suggested that the performance of the AI detection algorithm did not show a significant decline when used on advanced CT scan data, on which it was not specifically trained. Because larger datasets are more likely to include a wider feature distribution than smaller datasets, DL methods generated from larger datasets are expected to have more generalizability. Indeed, previous studies of DL algorithms for nonclassified tasks in medical imaging have found that larger multi-institutional development datasets improve their generalizability [20, 21]. Similar results on CPIs and VMIs could have been attributed to the commercial AI algorithm's extensive training on a huge dataset that included images from various CT systems.

In a recent study by Jungblut L et al., the AI-CAD system had comparable results for lung nodule detection and volume measurement between the photon-counting detector CT and the conventional energy-integrating detector CT (P=0.08–1.00), with an average sensitivity of 95% for the former and 86% for the latter [22]. X Zhu et al. reported that compared with single-energy CT, dual-energy CT may significantly improve the sensitivity of AI for the diagnosis of pulmonary nodules and is practical for the screening of pulmonary nodules in a large population [23]. Interestingly, Delong's test suggested that the diagnostic efficiencies of GGNs size (total volume and 3D long diameter) were slightly statistically different. These discrepancies may be due to the fact that VMIs improves soft tissue tumor image quality by simulated extrapolating photon energies to a desired kiloelectron volt (keV) level [24], within a certain range, the higher the keV level, the better the image quality

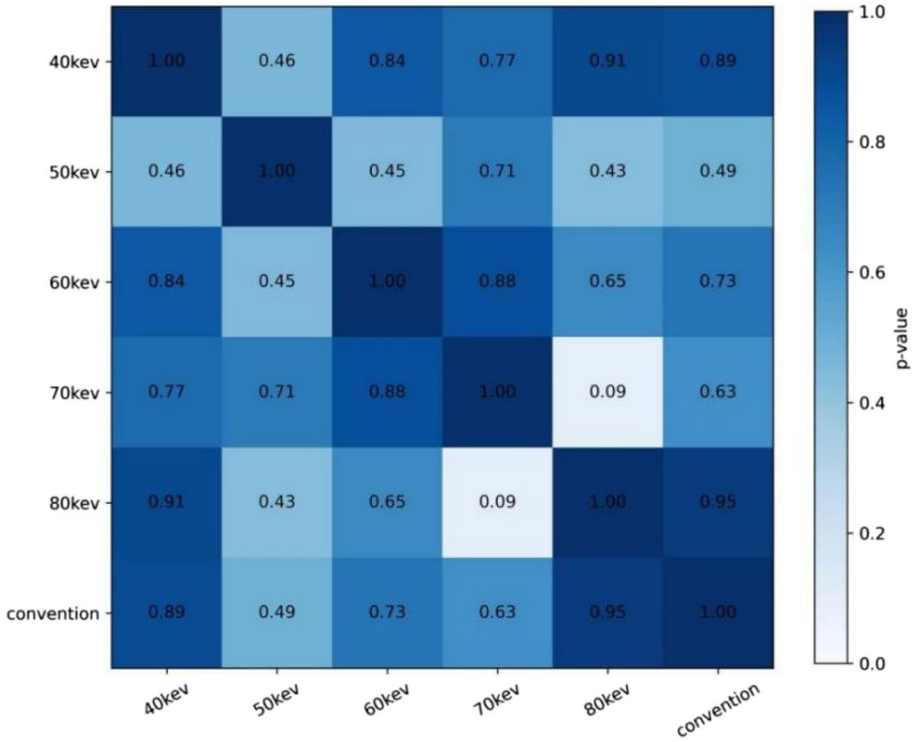

Fig. 3 Results of the Delong's test for ROC curves in total mass

Table 4 ROC curve analysis for identifying MIA from AIS in convention group and VMIs group

	AUC	95% CI	*P* value	Sensitivity	Specificity	Youden index	Cutoff value	DeLong test (vs. Convention)
3D long diameter								
Convention	0.665	0.546–0.785	0.009	70.50%	65.00%	0.355	7.37	—
80	0.665	0.544–0.786	0.010	70.50%	65.00%	0.355	7.37	0.95
70	0.659	0.539–0.779	0.012	72.70%	62.50%	0.352	7.17	0.63
60	0.660	0.540–0.781	0.012	72.70%	62.50%	0.352	7.37	0.73
50	0.654	0.532–0.778	0.015	70.50%	60.00%	0.305	7.25	0.49
40	0.663	0.542–0.785	0.010	68.20%	62.50%	0.307	7.35	0.89

3D Three-dimensional, *AIS* Adenocarcinomas in situ, *MIA* Minimally invasive adenocarcinoma, *VMIs* Virtual monochromatic images, *ROC* Receiver operating characteristic, *AUC* Area under curve, *CI* Confidence interval

of soft tissue lesions such as pulmonary nodules [16], head and neck cancer [25], gastric cancer [26], liver metastases [27], etc. In general, the observed high diagnostic accuracy of the AI algorithm for detecting pulmonary GGNs on VMIs is in line with previous studies on CPIs.

AI quantitative parameters for the diagnosis of pulmonary GGNs

With the application of deep learning, through AI, microscopic image information invisible to the naked eye can be extracted, and the features of GGNs can be quantitatively analyzed. Entropy can distinguish pre-invasive and invasive lung adenocarcinoma [28], and can predict the invasiveness of GGNs [29]. Increased tissue heterogeneity, image gray level inhomogeneity, and entropy can contribute to tumor growth. Entropy was an independent predictor for the diagnosis of AIS, MIC, or IAC, and the AUC can reach 0.90 [28]. The results of our study were also highly consistent with them. In our study, the AUC of entropy could reach 0.823 for the diagnosis of IAC

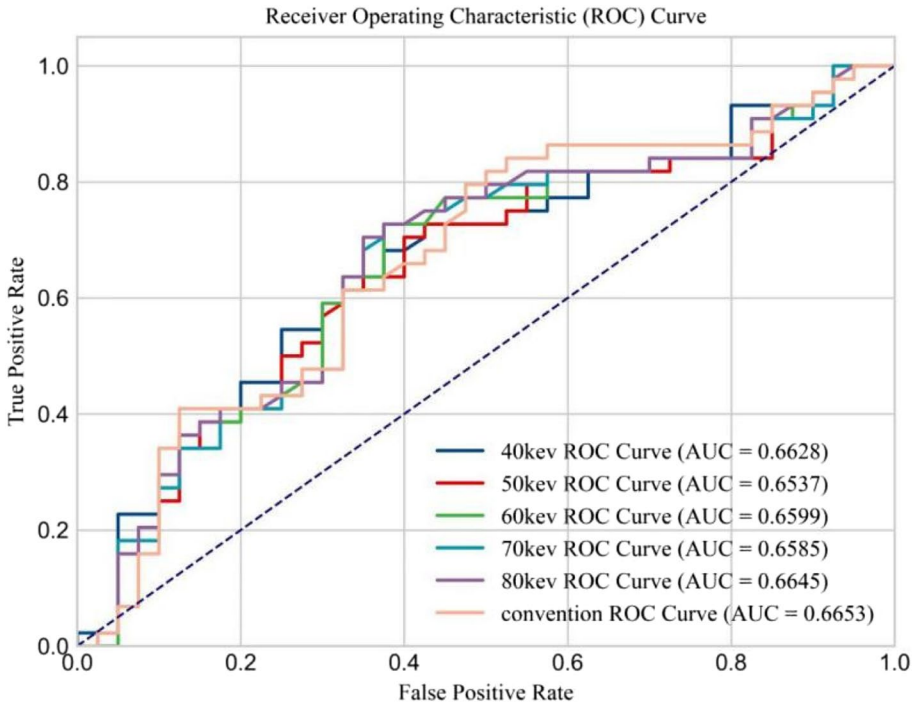

Fig. 4 Evaluation and verification of the MIA. ROC curves for 3D long diameter in the CPIs group and VMIs group. MIA, minimally invasive adenocarcinomas; ROC, receiver operating charcteristic; CPIs, computed tomography images; VMIs, virtual monochromatic images; 3D, three-dimensional

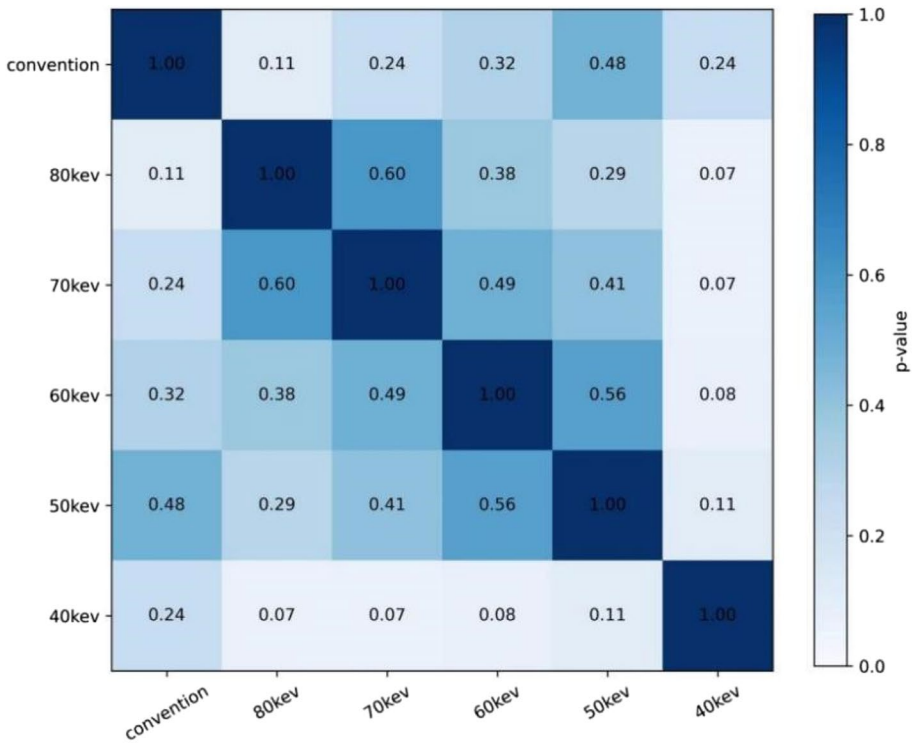

Fig. 5 Results of the Delong's test for ROC curves in 3D long diameter. 3D, three-dimensional

on CPIs. Logistic multivariable analysis indicated that total mass was a better quantitative index for differentiating IAC from MIA. Hyungjin Kim et al. [30] reported a similar finding that measuring the nodule total mass of pulmonary GGNs had an advantage over volumetric parameters. ROC analysis for differentiating invasive pulmonary adenocarcinomas among GGNs demonstrated that the AUC was highest for mass (0.792, 95% CI 0.691–0.872, $P<0.001$) (31). Hence, AI-based CT quantitative parameters are recommended for identifying microscopic image information between invasive (MIA, IAC) and pre-invasive lesions (AIS), improving diagnosis, and providing a reference for clinical precision treatment.

Identification of pulmonary GGNs on VMIs

We noticed that the diagnostic efficiencies of AI histogram parameters based on VMIs for invasive pulmonary nodules were slightly higher than those of CPIs, especially total mass and total volume. These differences were statistically significant, probably due to the fact that SDCT has outperformed traditional techniques and has various key advantages that include noise reduction, powerful post-processing functionality, etc. Studies on preclinical SDCT systems have shown promising results for the diagnosis of pulmonary nodules [31], with an improvement of image noise and CNR [32], as well as an improvement of texture information and shape owing to higher spatial resolution compared with conventional energy-integrating detector CT.

When pulmonary GGNs are encountered in clinical practice, 80 keV could be the optimal virtual monochromatic energy for the identification of preoperatively IAC on a non-enhanced chest CT. High keV VMIs from SDCT reduces beam hardening and metal artifacts that limit conventional CT interpretation. These artifacts, typically from x-ray beam interactions with metallic medical hardware, can obscure critical anatomy or pathology, limiting diagnostic certainty. Combining SDCT data with conventional CT algorithms can improve study quality and potentially save patients from additional radiation doses from repeat CT scans [33]. Whereas, our results were not consistent with the previous study of image quality with SDCT in lung cancer by Weishu H et al. [17]. According to their research results, the combination of 60 and 70 keV virtual monochromatic spectral images in SDCT results in a significantly superior CNR, inhomogeneity evaluation, and subjective image quality evaluation for lung cancer detection [17]. This discrepancy may be due to their study used contrast-enhanced chest scans on pulmonary GGNs, while ours used non-enhanced CT. Theoretically, the attenuation of iodine is greater at lower energies than at higher energies, due to the increasing photoelectric absorption that occurs with decreasing photon energies [34]. Nevertheless, we have shown that higher keV could be the optimal virtual monochromatic energy for the identification of IAC on a non-enhanced CT chest scan, which is worthy of clinical application. Experience with the application of AI based on VMIs technique training in the identification of pulmonary GNNs is still scarce, future studies are required. SDCT can be a good choice for patients with poor respiratory training who need a chest CT scan.

Limitations

There were some limitations to this study. First, our study did not specifically focus on the analysis of objective and subjective image qualities, the effect of such improved lesion SNR and CNR on diagnostic accuracy remains unknown. Second, we did not analyze the solid component and morphological characteristics of pulmonary GGNs. In clinical diagnosis,an accurate grasp of the imaging manifestations of pulmonary ground-glass nodules is helpful to clinical diagnosis and effectively avoids missed diagnosis and misdiagnosis [35, 36]. Finally, due to the small sample size included in this study and the single-center nature of this study, further studies with more patients are needed to verify our results.

Conclusion

In summary, the AI algorithm trained on CPIs showed consistent diagnostic performance on VMIs, indicating its usefulness in clinical practice for differential diagnosis of pulmonary GGNs. When pulmonary GGNs are encountered in clinical practice, 80 keV could be the optimal virtual monochromatic energy for the identification of preoperatively IAC on a non-enhanced chest CT.

Abbreviations

GGNs	Pulmonary ground-glass nodules
HRCT	High-resolution computed tomography
AIS	Adenocarcinomas in situ
MIA	Minimally invasive adenocarcinomas
IAC	Invasive adenocarcinomas
AI	Artificial intelligence
SDCT	Dual-layer detector spectral computed tomography
VMIs	Virtual monochromatic images
CPIs	Conventional polychromatic computed tomography images
CT	Computed tomography
SNR	Signal-to-noise ratio
CNR	Contrast-to-noise ratio
DL-CAD	Deep learning-based computer-aided diagnosis
SBI	Spectral base images
3D	Three-dimensional
AUC	The area-under the curve
ROC	Receiver operating characteristic
OR	Odds ratio
CI	Confidence interval

Supplementary Information

The online version contains supplementary material available at https://doi.org/10.1186/s12880-024-01467-2.

Supplementary Material 1.

Supplementary Material 2.

Supplementary Material 3.

Supplementary Material 4.

Acknowledgements
We thank all the authors that contributed to this work.

Clinical trial number
Not applicable.

Methodology
Retrospective; Diagnostic or prognostic study.

Guarantor
The scientific guarantor of this publication is Dan Han.

Authors' contributions
Acquisition, analysis, or interpretation of data: Shaolei Kang, Zhongyan Ma, Hui Duan, Li-chang Lei. Drafting of the manuscript: Shaolei Kang, Zhongyan Ma, Wei-wei Jing. Critical revision of the manuscript for important intellectual content: Hai-lin Zhang, Dan, Han, Qin Song. Approved final manuscript: Fa-jin Lv, Wei Zhao.

Funding
This research was supported by the National Key R&D Program of China (No. 2020YFA0714002), and Chongqing Technology Innovation and Application Development Projects (No. CSTC2021jscx-gksb-N0030), and Chongqing Science and Health Joint Medical Research Project (No. 2022ZDXM006), and Chongqing Health Appropriate Technology Promotion Project (No. 2023jstg044), Fajin Lv; the Yunnan Province Special Fund of Clinical Research Center of Radiology and Therapy of China (No. 202102AA100067), Wei Zhao.

Data availability
All data generated or analysed during this study are included in this published article [and its supplementary information files].

Declarations

Ethics approval and consent to participate
The authors are accountable for all aspects of the work, ensuring that questions related to the accuracy or integrity of any part of the work were appropriately investigated and resolved. This study conformed to the Declaration of Helsinki on Human Research Ethics standards and was approved by the institutional review board of the First Affiliated Hospital of Kunming Medical University (No.2022-L179).The need for written informed consent was waived because of the retrospective study.

Consent for publication
Not applicable.

Competing interests
The authors declare no competing interests.

Author details
[1]Department of Radiology, First Affiliated Hospital of Kunming Medical University, 295Xichang Road, Wuhua, Kunming 650032, China. [2]Department of Radiology, Yunnan Cancer Center, Yunnan Cancer Hospital, The Third Affiliated Hospital of Kunming Medical University, Kunming 650118, China. [3]Department of Radiology, First Affiliated Hospital of Chongqing Medical University, 1 Youyi Rd, Yuanjiagang, Yuzhong, Chongqing 40016, China.

Received: 31 July 2024 Accepted: 16 October 2024
Published online: 29 October 2024

References

1. Huang J, Deng Y, Tin MS, et al. Distribution, risk factors, and temporal trends for lung cancer incidence and mortality: a global analysis. Chest. 2022;161(4):1101–11.
2. Ye T, Deng L, Xiang J, et al. Predictors of pathologic tumor invasion and prognosis for ground glas-s opacity featured lung adenocarcinoma. Ann Thorac Surg. 2018;106(6):1682–90.
3. Cai Y, Chen T, Zhang S, Tan M, Wang J. Correlation exploration among CT imaging, pathology and genotype of pulmonary ground-glass opacity. J Cell Mol Med. 2023;27(14):2021–31.
4. Sheshadri A, Rodriguez A, Chen R, et al. Effect of reducing field of view on multidetector quantitative computed tomography parameters of airway wall thickness in asthma. J Comput Assist Tomogr. 2015;39(4):584–90.
5. Kunihiro Y, Tanaka N, Kawano R, et al. Differentiation of pulmonary complications with extensive ground-glass attenuation on high-resolution CT in immunocompromised patients. Jpn J Radiol. 2021;39(9):868–76.
6. Nicholson AG, Tsao MS, Beasley MB, et al. The 2021 WHO classification of lung tumors: impact of advances since 2015. J Thorac Oncol. 2022;17(3):362–87.
7. Yotsukura M, Asamura H, Motoi N, et al. Long-term prognosis of patients with resected adenocarcinoma in situ and minimally invasive adenocarcinoma of the lung. J Thorac Oncol. 2021;16(8):1312–20.
8. Kay FU, Kandathil A, Batra K, Saboo SS, Abbara S, Rajiah P. Revisions to the tumor, node, metastasis staging of lung cancer (8th edition): rationale, radiologic findings and clinical implications. World J Radiol. 2017;9(6):269–79.
9. Dai J, Yu G, Yu J. Can CT imaging features of ground-glass opacity predict invasiveness? A meta-analysis. Thorac Cancer. 2018;9(4):452–8.
10. Cui S, Ming S, Lin Y, et al. Development and clinical application of deep learning model for lung nodules screening on CT images. Sci Rep. 2020;10(1):13657.
11. Gao R, Gao Y, Zhang J, Zhu C, Zhang Y, Yan C. A nomogram for predicting invasiveness of lung adenocarcinoma manifesting as pure ground-glass nodules: incorporating subjective CT signs and histogram parameters based on artificial intelligence. J Cancer Res Clin Oncol. 2023;149(17):15323–33.
12. Yacoub B, Varga-Szemes A, Schoepf UJ, et al. Impact of artificial intelligence assistance on chest CT interpretation times: a prospective randomized study. Am J Roentgenol. 2022;219(5):743–51.
13. Do TD, Rheinheimer S, Kauczor HU, Stiller W, Weber T, Skornitzke S. Image quality evaluation of dual-layer spectral CT in comparison to single-layer CT in a reduced-dose setting. Eur Radiol. 2020;30(10):5709–19.
14. van Ommen F, de Jong HWAM, Dankbaar JW, Bennink E, Leiner T, Schilham AMR. Dose of CT protocols acquired in clinical routine using a dual-layer detector CT scanner: a preliminary report. Eur J Radiol. 2019;112:65–71.
15. Kim C, Kim W, Park SJ, et al. Application of dual-energy spectral computed tomography to thoracic oncology imaging. Korean J Radiol. 2020;21(7):838–50.
16. Kaup M, Scholtz JE, Engler A, et al. Dual-energy computed tomography virtual monoenergetic imaging of lung cancer: assessment of optimal energy levels. J Comput Assist Tomogr. 2016;40(1):80–5.
17. Hou W, Sun X, Yin Y, et al. Improving image quality for lung cancer imaging with optimal monochromatic energy level in dual energy spectral computed tomography. J Comput Assist Tomogr. 2016;40(2):243–7.
18. Wu Z, Wang F, Cao W, et al. Lung cancer risk prediction models based on pulmonary nodules: a systematic review. Thoracic cancer. 2022;13(5):664–77.
19. Yu AC, Mohajer B, Eng J. External validation of deep learning algorithms for radiologic diagnosis: a systematic review. Radiol Artif Intell. 2022;4(3):e210064.
20. Remedios SW, Roy S, Bermudez C, et al. Distributed deep learning across multisite datasets for generalized CT hemorrhage segmentation. Med Phys. 2020;47(1):89–98.

21. Balki I, Amirabadi A, Levman J, et al. Sample-size determination methodologies for machine learning in medical imaging research: a systematic review. Can Assoc Radiol J. 2019;70(4):344–53.
22. Jungblut L, Blüthgen C, Polacin M, et al. First performance evaluation of an artificial intelligence-based computer-aided detection system for pulmonary nodule evaluation in dual-source photon-counting detector ct at different low-dose levels. Invest Radiol. 2022;57(2):108–14.
23. Zhu X, Zhu L, Song D, Wang D, Wu F, Wu J. Comparison of single- and dual-energy CT combined with artificial intelligence for the diagnosis of pulmonary nodules. Clin Radiol. 2023;78(2):e99–105.
24. Leng S, Yu L, Fletcher JG, McCollough CH. Maximizing iodine contrast-to-noise ratios in abdominal CT imaging through use of energy domain noise reduction and virtual monoenergetic dual-energy CT. Radiology. 2015;276(2):562–70.
25. Wichmann JL, Nöske EM, Kraft J, et al. Virtual monoenergetic dual-energy computed tomography: optimization of kiloelectron volt settings in head and neck cancer. Invest Radiol. 2014;49(11):735–41.
26. Li C, Shi C, Zhang H, Hui C, Lam KM, Zhang S. Computer-aided diagnosis for preoperative invasi-on depth of gastric cancer with dual-energy spectral CT imaging. Acad Radiol. 2015;22(2):149–57.
27. Sudarski S, Apfaltrer P, Nance JW, et al. Objective and subjective image quality of liver parenchyma and hepatic metastases with virtual monoenergetic dual-source dual-energy CT reconstructions: an analysis in patients with gastrointestinal stromal tumor. Acad Radiol. 2014;21(4):514–22.
28. Yagi T, Yamazaki M, Ohashi R, et al. HRCT texture analysis for pure or part-solid ground-glass nodules: distinguishability of adenocarcinoma in situ or minimally invasive adenocarcinoma from invasive adenocarcinoma. Jpn J Radiol. 2018;36(2):113–21.
29. Yang Y, Wang WW, Ren Y, et al. Computerized texture analysis predicts histological invasiveness within lung adenocarcinoma manifesting as pure ground-glass nodules. Acta Radiol. 2019;60(10):1258–64.
30. Kim H, Goo JM, Park CM. Evaluation of T categories for pure ground-glass nodules with semi-automatic volumetry: is mass a better predictor of invasive part size than other volumetric parameters? Eur Radiol. 2018;28(10):4288–95.
31. Leng S, Yu Z, Halaweish A, et al. Dose-efficient ultrahigh-resolution scan mode using a photon counting detector computed tomography system. J Med imaging (Bellingham, Wash). 2016;3(4):043504.
32. Symons R, Pourmorteza A, Sandfort V, et al. Feasibility of dose-reduced Chest CT with Photon-counting detectors: initial results in humans. Radiology. 2017;285(3):980–9.
33. Gupta A, Kikano EG, Bera K, et al. Dual energy imaging in cardiothoracic pathologies: a primer for radiologists and clinicians. Eur J Radiol Open. 2021;8:100324.
34. Frellesen C, Kaup M, Wichmann JL, et al. Noise-optimized advanced image-based virtual monoenergetic imaging for improved visualization of lung cancer: comparison with traditional virtual monoenergetic imaging. Eur J Radiol. 2016;85(3):665–72.
35. Hu H, Wang Q, Tang H, Xiong L, Lin Q. Multi-slice computed tomography characteristics of solitary pulmonary ground-glass nodules: differences between malignant and benign. Thorac Cancer. 2016;7(1):80–7.
36. Snoeckx A, Reyntiens P, Desbuquoit D, et al. Evaluation of the solitary pulmonary nodule: size matte-rs, but do not ignore the power of morphology. Insights Imaging. 2018;9(1):73–86.

Publisher's Note